Solar Energy 314 (2026) 114733

Contents lists available at ScienceDirect

Solar Energy

journal homepage: www.elsevier.com/locate/solener

Indoor PF2:ITIC organic solar cells with enhanced blue-light harvesting and high voltage

Ruoxue He [a], Nicolas Leclerc [b], Pierre Nickmilder [c], Philippe Leclère [c], Bernard Ratier [a], Johann Bouclé [a,*]

[a] XLIM, Université de Limoges, CNRS, UMR 7252, F-87000 Limoges, France
[b] Institut de Chimie et Procédés pour l'Energie, l'Environnement et la Santé (ICPEES), Université de Strasbourg, CNRS, UMR 7515, 67087 Strasbourg, France
[c] Laboratoire de Physique des Nanomatériaux et Energie (LPNE), Institut de recherche en Sciences et Ingénierie des Matériaux, Université of Mons B-7000 Mons, Belgium

ARTICLE INFO

Keywords:
Organic solar cells
Indoor energy harvesting
Non-fullerene acceptors
Internet of things (IoT)
Indoor photovoltaics
Bulk-heterojunction

ABSTRACT

Organic photovoltaic (OPV) devices designed for indoor applications require active materials matching the optical emission of artificial lighting in the 400–750 nm range while allowing high open-circuit voltage (V_{OC}) under low illumination intensity. In this study, the combination of the fluorinated polymer donor PF2, which exhibits a very specific absorption in the blue region, and the non-fullerene acceptor ITIC is investigated to develop efficient indoor OPV devices. The effects of solvent selection and active layer thickness on device performance were systematically explored. Among the solvents tested, chlorobenzene produced the most uniform and defect-free blend film morphology, enabling efficient exciton dissociation and charge transport. To better link morphology and performance, we employed scanning microwave impedance microscopy (sMIM), here applied for the first time to an organic photovoltaic system. By increasing the active layer thickness from 100 nm to 270 nm, the absorption in the blue region (400–500 nm) is significantly enhanced, thereby increasing the generated photocurrent by taking advantage of the blue emission of the indoor warm white LED source considered. Consequently, the optimized PF2:ITIC device achieves a power conversion efficiency of nearly 12% and a significant V_{OC} of 0.72 V under 1000 lx. The PF2:ITIC blends exhibited stable morphology and high performance at different thicknesses, making them promising candidates for scalable printed OPVs targeting indoor energy harvesting for Internet-of-things (IoT) devices.

1. Introduction

The growing demand for low-power Internet of Things (IoT) devices for indoor applications is driving advancements in ultra-low-power electronics and high-performance indoor photovoltaic (IPV) systems. Solar energy offers a sustainable and cost-effective solution, aligning with global environmental goals while reducing the carbon footprint of IoT systems [1–3]. Among emerging technologies, organic solar cells (OSCs) based on the bulk-heterojunction (BHJ) concept have shown great promise for powering indoor IoT devices due to their high tunability, flexibility, and cost-effectiveness [4,5]. Additionally, scalable roll-to-roll processing and encapsulation have been demonstrated for indoor OPV modules. This demonstrates the practical relevance of OPVs for powering low-power sensors under ambient illumination [6]. Recent developments, particularly in non-fullerene acceptors (NFAs), have enabled OSCs to achieve impressive power conversion efficiencies (PCEs) exceeding 36% under 1000 lx LED illumination [7], surpassing conventional monocrystalline silicon cells, which typically reach around 9.65% under similar conditions [8], and approaching the performance of perovskite-based devices, which have reported PCEs as high as 45.51% under indoor lighting [9].

Indoor artificial lighting sources, such as fluorescent lamps (FLs) and white LEDs, emit light primarily in the 400–750 nm range, with significantly lower intensity than standard solar illumination (AM 1.5G). While AM 1.5G provides typical irradiance levels of 100 mW/cm^2, indoor artificial light intensities lead to values below 1 mW/cm^2, making them 100 to 1000 times weaker than sunlight. Due to these differences in spectrum and intensity, the optimal requirements for OSCs under indoor conditions differ from outdoor applications (Fig. 1a), with device performance predominantly influenced by trap-assisted recombination [9,10]. The Shockley-Queisser limit suggests that for optimal indoor performance of single junction devices, active layer materials should

* Corresponding author.
E-mail address: johann.boucle@unilim.fr (J. Bouclé).

https://doi.org/10.1016/j.solener.2026.114733
Received 3 October 2025; Received in revised form 19 January 2026; Accepted 21 May 2026
Available online 25 May 2026

have bandgaps of approximately 1.9–2.0 eV, which theoretically allows for maximum PCEs of around 60% under artificial lighting [11,12]. Thus, photoactive materials for indoor OSCs should possess large to medium bandgaps with narrow absorption spectra in the visible range to effectively harvest photons from artificial light while enabling high open-circuit voltage (V_{OC}).

In this context, substantial progress has been achieved through the development of NFAs and the optimization of blend morphology via molecular design and processing control. These strategies involve the modification of halogen elements, end groups and side chains to adjust the energy levels, change the light absorption range and improve the morphology of the active layer. For example, within the ITIC family (known as 3,9-bis(2-methylene-(3-(1,1-dicyanomethylene)-indanone))-5,5,11,11-tetrakis(4-hexylphenyl)-dithieno[2,3-d:2′,3′-d’]-s-indaceno [1,2-b:5,6-b’]dithiophene), variants such as ITIC, IO-4Cl, IT-4F and IT-M have been explored. In 2019, Ding's research group [13] constructed an OPV device based on CD1:ITIC. The device showed a V_{OC} of 0.78 V, a Jsc of 116 μA/cm^2, an FF of 68.1%, and a P_{OUT} of 62 μW/cm^2, resulting in a PCE of 17.9% under FL illumination at 1000 lx. Similarly, Cui *et al.* [14] developed a new NFA, IO-4Cl, which was blended with PM6 to achieve a high PCE of 26.1% and a V_{OC} of 1.1 V under warm LED illumination of 1000 lx. Further, the materials IT-4F and IT-M, when blended with PM6 and characterized under LED conditions, achieved PCEs of up to 15.03% [15] and 22.8% [16], respectively. Despite recent advancements in acceptor materials, a significant challenge for OPVs remains the effective utilization of higher-energy photons, particularly the blue region of indoor LED lighting based on gallium nitride emitters, while maintaining a high V_{OC} at low irradiance. Many conventional donor/acceptor systems do not fully exploit this blue component under low-intensity indoor conditions, which can limit photocurrent and voltage. In addition, some high-performing NFAs have been reported to be vulnerable under blue-rich illumination [17,18]. Moreover, maintaining a high V_{OC} at low irradiance requires minimizing low-light loss processes, such as trap-assisted recombination [19]. Consequently, there remains a strong interest in donor materials that can effectively utilize high-energy photons and remain stable under blue-light-rich illumination, as well as complementary characterization methods that can enhance the morphology-performance correlation in indoor OPVs.

In this study, we investigate the fluorinated polymer donor PF2 (Fig. 2a) as a promising candidate to address this challenge [20–22]. PF2 satisfies the critical requirements for indoor OPVs, featuring a medium bandgap and strong absorption spectrum ranging from 400 to 750 nm (Fig. 2b), which aligns well with the emission spectra of indoor artificial light sources (400–730 nm), making it highly effective at harvesting light from indoor LED sources. PF2 also exhibits favorable molecular energy levels and the ability to self-organize into crystalline lamellae, forming a mixed face-on/edge-on orientation that facilitates enhanced charge transport. Moreover, it demonstrates good compatibility with both fullerene-based acceptors such as $PC_{71}BM$ and NFA like Y6, underscoring its versatility for OPV device optimization. In 2019, Ibraikulov *et al.* [21] reported a PCE of 10.5%, a V_{OC} of 0.75 V, a J_{SC} of 19.5 mA/cm^2, and a FF of 72% using a PF2:$PC_{71}BM$ system under full sun. Based on this, Ma *et al.* [22] further improved the PF2-based system in 2020 by introducing a ternary mixture containing two polymer donors. This approach minimizes energy losses and achieves a PCE of 12.12%, a J_{SC} of 24.97 mA/cm^2, a FF of 64.70%, and a V_{OC} of 0.75 V (still under full sun). However, these studies mainly focus on outdoor lighting conditions, and the potential of PF2-based systems under indoor lighting remains to be explored. To complement PF2, we selected ITIC as electron acceptor [23–26] (Fig. 2a), a widely studied NFA known for its excellent charge separation and transport properties. This PF2:ITIC blend is specifically tailored to optimize light absorption and enhance photocurrent generation under indoor LED illumination (Fig. 2b). To maximize photovoltaic performance, we systematically study the effects of solvent selection, donor-to-acceptor ratio, and active layer thickness on film formation. Importantly, to strengthen the link between morphology and performance, we employed sMIM to probe local electrical heterogeneity in hybrid thin films, it’s first application of this technique to an organic photovoltaic system. This combined approach allows us to determine the processing conditions for obtaining a uniform, defect-free morphology and to elucidate how the increased blue light absorption due to thickness translates into improved indoor photocurrent and efficiency.

2. Experimental details

2.1. Materials

The polymer donor PF2, a di-fluorinated copolymer donor based on thienothiophene and a difluorinated benzothiadiazole moiety with two thiophene units substituted by two octyl-dodecyl alkyl side chains at the β-position, has been synthesized according to reported procedures [20]. ITIC was purchased commercially from Ossila Ltd. (UK). Their chemical structures, absorption spectra, and energy levels (the highest occupied molecular orbital or HOMO and the lowest unoccupied molecular orbital or LUMO) are given in Fig. 2a–c, respectively. The absorption spectra were recorded by UV–Vis spectroscopy on thin films prepared under the same conditions as those used for device fabrication. The HOMO and LUMO energy levels were extracted from the literature [20,27], based on cyclic voltammetry and the value of optical band gap. Indium tin oxide (ITO)-coated substrates with 7 Ω/sq were purchased from VisionTek Systems Ltd (UK). Zinc oxide (ZnO) nanoparticle colloidal solution (5 nm diameter, ZnO 1% wt. semiconductive ink for inkjet printing) was supplied by Genes’Ink under the product name “Hélio ETL Jet”. Molybdenum(VI) oxide (MoO_3, purity 99.97%) was purchased from Merck KGaA (Germany). Silver (Ag, purity 99.99%) was

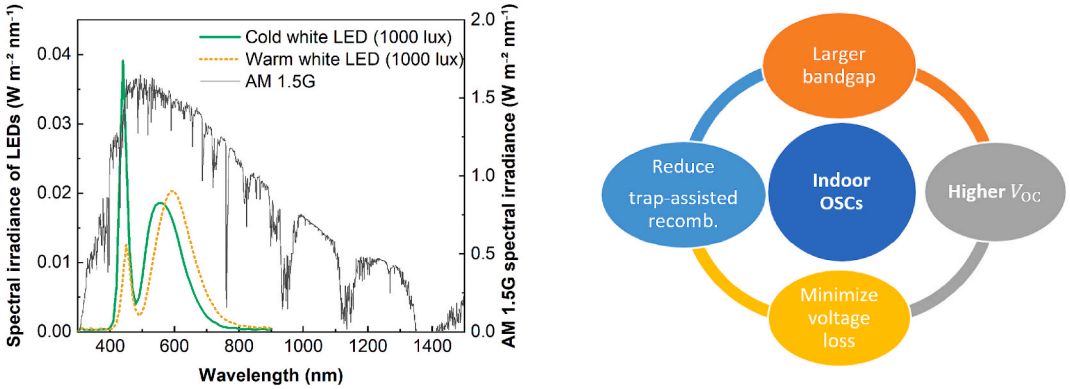

Fig. 1. (a) Spectral irradiance of cold white and warm white LEDs at 1000 lx (left axis) compared to the AM 1.5G solar spectrum (right axis). (b) Key parameters to optimize indoor organic solar cell performance.

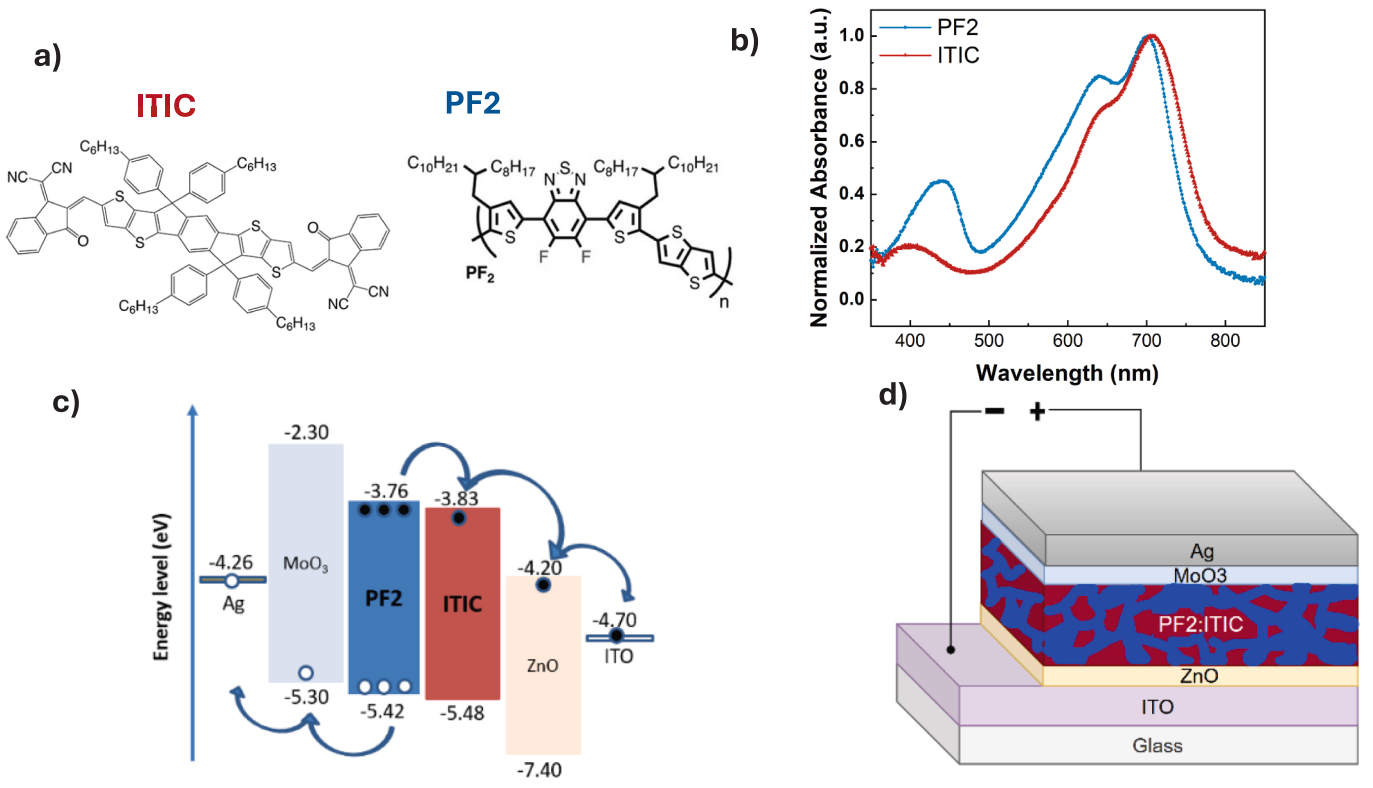

Fig. 2. (a) Chemical structures of the donor polymer PF2 and the non-fullerene acceptor ITIC. (b) Normalized absorption spectra of PF2 and ITIC in thin films. (c) Energy level diagram of the materials used in the device architecture. (d) Schematic diagram of the inverted organic solar cell structure used in this study.

purchased in the form of a 0.5 mm diameter filament from Goodfellow. Chlorobenzene (CB, anhydrous, 99.8%), *ortho*-dichlorobenzene (o-DCB, anhydrous, 99.8%), chloroform (CF, anhydrous, 99.8%) were all purchased from Merck KGaA (Germany) and used as received.

2.2. Photovoltaic device fabrication

Solar cells with PF2:ITIC active layer were fabricated using an inverted architecture: glass/ITO/ZnO/PF2:ITIC/MoO_3/Ag, as shown in Fig. 2d. ITO-coated glass substrates were etched using hydrochloric acid, cleaned with subsequent ultrasonic baths in solvents (acetone, ethanol, isopropyl alcohol) and coated in air with a 20 nm ZnO layer by spin-coating at 4000 rpm for 40 s. The films were then annealed in open air at 130 °C for 10 min to remove residual solvents and organic materials. The ZnO-coated substrates were then transferred to a nitrogen-filled glove box where the PF2:ITIC active layer was deposited with a donor to acceptor (D:A) mass ratio of 1:1.5. Considering the molar mass of the PF2 repeat unit (1033.66 g/mol) and the molecular weight of ITIC (1427.94 g/mol), the selected mass ratio of 1:1.5 corresponds approximately to a close to 1:1 M ratio between one PF2 repeat unit and one ITIC molecule. Blends were initially prepared using three different solvents: CB, CF and o-DCB. In each case, the processing parameters were optimized to obtain active layers of approximately 100 nm thickness. Detailed formulations and processing conditions for each solvent system are given in the Supporting Information. Finally, 10 nm of MoO_3 and 100 nm of Ag were thermally evaporated as the hole transport layer and top electrode, respectively, under high vacuum ($\sim 10^{-6}$ mbar). The active device area was 0.18 cm^2 defined by a shadow mask.

2.3. Characterization

The surface morphology of the thin films was investigated using scanning electron microscopy (SEM) and atomic force microscopy (AFM). AFM measurements were performed using a Bruker Dimension Icon operating in PeakForce Tapping quantitative nanomechanics (PFT-QNM) mode. This mode is simultaneously providing, on top of topography, the map of adhesion, deformation, and indentation [28]. Silicon cantilevers (AppNano ACTA-50, nominal spring constant k = 13–77 N/m, resonance frequency f_0 = 200–400 kHz, tip radius <10 nm, Al reflex coating) were used. A PeakForce setpoint of 20 nN was applied to avoid sample damage. To probe the nanoscale electrical properties of the active layer, we employed scanning microwave impedance microscopy (sMIM), an advanced AFM-based technique capable of mapping local capacitance (sMIM-C) and resistance (sMIM-R). The sMIM measurements were performed using the same Bruker system equipped with sMIM module (PrimeNano Inc.) and specialized coaxially shielded AFM probes (PrimeNano SMIM-150, Si_3N_4 cantilever, k ≈ 8 N/m, f_0 ≈ 75 kHz, TiW/Au shielding), specifically designed for microwave impedance microscopy [29,30]. The optoelectronic properties of the active layer were characterized by ultraviolet–visible (UV–vis) absorption spectroscopy and photoluminescence (PL) measurements. UV–vis spectra were recorded using an Agilent Technologies Cary 300 spectrometer equipped with an integrating sphere, covering the spectral range of 200–800 nm. PL spectra were acquired using an Edinburgh FLS980 photoluminescence spectrometer using a monochromated 450 W Xenon lamp as excitation source and a R928P Peltier-cooled photomultiplier. Current density–voltage (J-V) measurements were carried out inside a nitrogen-filled glove box using a computer-controlled Keithley 2400 sourcemeter. Under outdoor conditions, a solar simulator (K.H. Steuernagel Lichttechnik GmbH) calibrated with a Newport Oriel SN 10510–0021 reference cell was used to simulate AM 1.5G illumination of 100 $mW.cm^{-2}$. Standard mismatch correction protocols were applied. For indoor testing, J-V measurements were standardized at 200, 500, and 1000 lx using LED light sources to ensure consistency and comparability with IEC indoor standard [31]. The measurements were performed inside a custom-built black box with black walls and black aperture to minimize reflections and the LED-to-sample distance was fixed. The lighting level was controlled using an ISO-TECH IPS 303DD

power supply, with detailed settings given in Table S1 (Supporting Information). To ensure accurate quantification of illumination and optical power density, we used a BLACK-Comet Super Range 200–1100 nm spectrometer (StellarNet Inc., USA) equipped with a cosine-corrected detector located at the same distance from the device under test. IPCE spectra were recorded using an ENLITECH QE-T system, providing wavelength-resolved insights into the photocurrent generation efficiency over the effective spectral range of the device.

3. Results and discussion

PF2:ITIC thin films were initially deposited on ITO/ZnO substrates following the experimental procedure depicted in the experimental section. As seen from SEM and AFM analysis (Fig. 3), PF2:ITIC blend films show large-scale uniformity and nanoscale structural variations depending on the solvent used for active layer processing. Notably, the films processed from CB exhibited a smooth and uniform surface morphology, whereas those processed from CF and o-DCB showed obvious aggregates (Fig. 3 top row). These large-scale features are particularly present in the CF-processed films, which are attributed to the poor solubility of PF2 in CF and its low boiling point (61 °C), leading to rapid solvent evaporation and incomplete phase mixing (polymer aggregates). To help confirm verify this assumption, we applied the Hansen Solubility Parameter (HSP) theory [32] to evaluate the compatibility of PF2 with each solvent (see detailed calculations and parameter values in Supporting Information). The calculated relative energy difference (RED) values showed that CB (RED = 0.25) and o-DCB (RED = 0.62) were within the solubility limit (RED < 1), indicating good compatibility with PF2. In contrast, CF (RED = 1.00) was exactly at the threshold, suggesting only partial solubility. For CB and o-DCB, the RED values were less than 1, indicating that PF2 was highly soluble in these solvents, with CB showing the highest compatibility. These results are consistent with the observed film morphologies, reinforcing the correlation between solvent compatibility and film quality.

AFM topography images further confirmed the nanoscale differences in surface morphology (Fig. 3, middle row). The root mean square (RMS) roughness increases from CF (1.88 nm) to CB (1.98 nm) and significantly increases to o-DCB (22.3 nm). These variations can be correlated with

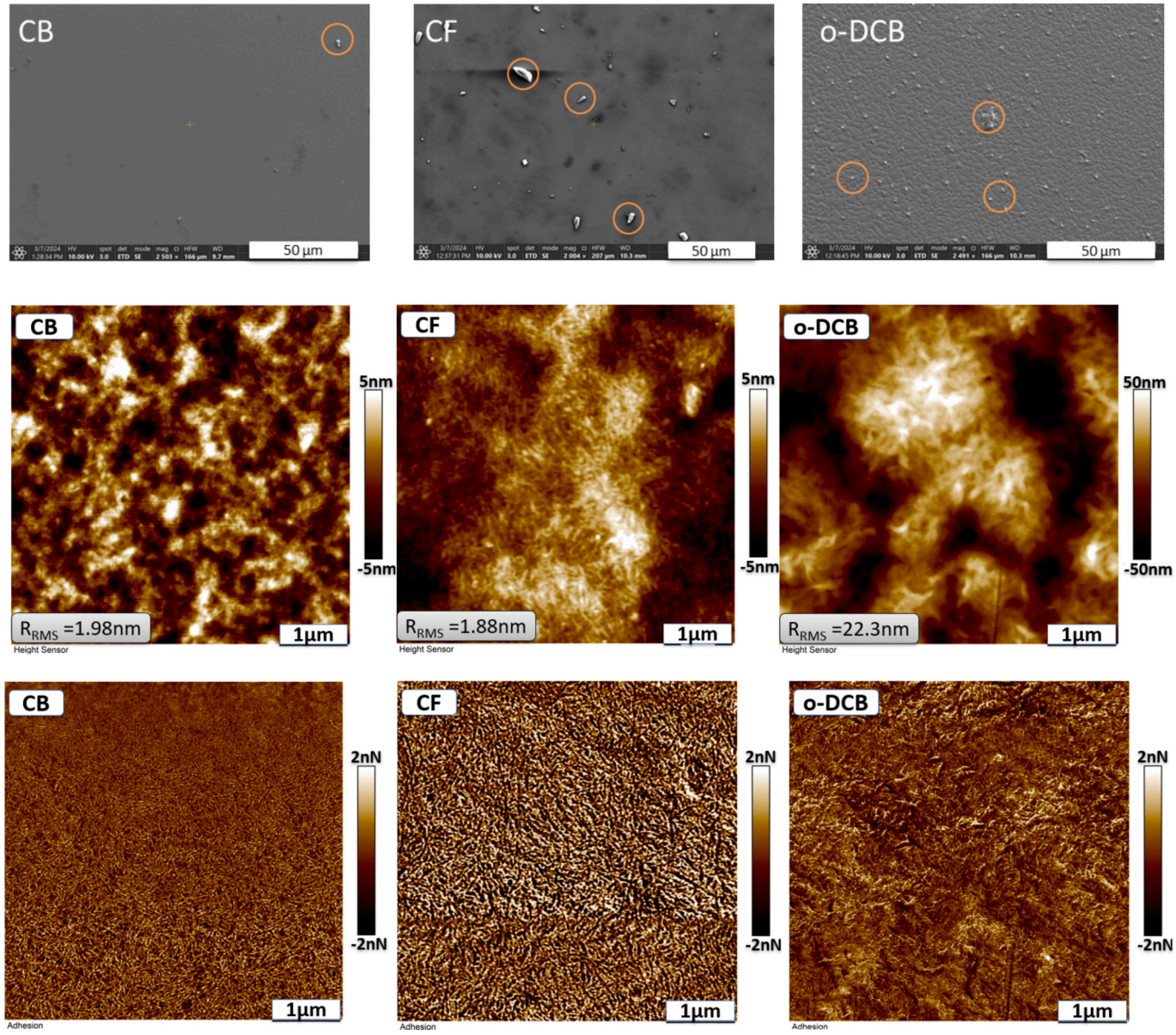

Fig. 3. SEM images (top row), AFM topography images (5 × 5 µm, middle row), and AFM adhesion images (5 × 5 µm, bottom row) of PF2:ITIC blend films of CB, CF, and o-DCB.

solvent properties such as boiling point, evaporation rate, and solubility. The CB film benefits from a moderate evaporation rate (boiling point: 132 °C), promoting controlled phase separation and a uniform morphology. While the CF-processed film shows the lowest roughness in the AFM scan, this apparent smoothness results from measurements taken in regions that exclude large aggregates. SEM observations reveal the presence of micron-sized clusters in the CF film, indicating inhomogeneity at a larger scale. The fast evaporation of CF (boiling point: 61 °C) tends to trap these aggregates during film formation, compromising film uniformity, and potentially device performance (see next sections of the article). On the other hand, o-DCB, with a higher boiling point (179 °C), induces excessive molecular rearrangement and phase separation, resulting in increased roughness and coarse domains. AFM adhesion images revealed the presence of an interpenetrating network structure in all three films (Fig. 3, bottom row). However, domain size and contrast vary depending on the solvent. The CB-treated film showed small, evenly distributed domains with minimal contrast, indicating good donor–acceptor phase mixing. In contrast, the CF film shows more defined and slightly larger domains, which may suggest better local nanoscale ordering, but this does not reflect the overall film morphology due to the presence of larger-scale aggregates. The o-DCB film showed irregular rough domains, which might be the result of excessive crystallization due to slow solvent evaporation. These large and isolated domains may hinder efficient charge transport by disrupting percolation pathways and increasing recombination. Therefore, the morphology and solubility data suggest that CB-treated PF2:ITIC films offer the most favorable nanostructure for high-performance organic solar cells. In contrast, the large aggregates and irregular phase separation present in CF and o-DCB films may limit the charge transport, favor charge recombination, and reduce the overall device efficiency.

To gain deeper insight into the correlation between film morphology and local electronic properties, we employed scanning microwave impedance microscopy (sMIM) on PF2:ITIC hybrid films treated with different solvents. To the best of our knowledge, this is the first time that sMIM has been applied to a conjugated polymer-based system. This technique simultaneously maps nanoscale variations in capacitance and conductivity, allowing us to probe dielectric uniformity and phase distribution within the film. The sMIM images (Fig. 4) show that films treated with CB and CF exhibit uniform contrast in both capacitance and conductance channels, indicating well-mixed morphologies and spatially uniform electrical properties. These observations are consistent with the AFM and SEM results, confirming that CB and CF promote the formation of continuous, low-roughness films. In contrast, films treated with o-DCB show a clear phase separation characterized by drastic local changes in dielectric and conductive signals. This observation is consistent with the larger domain sizes seen in AFM and SEM, indicating extensive donor–acceptor separation due to the slow evaporation rate of o-DCB. Further insights were obtained from sMIM conductivity images of o-DCB treated films, thanks to its very specific features. Elongated high conductivity domains were identified, which can be attributed to the PF2 polymer chains. The estimated lengths of these features (92, 105, and 132 nm) agree well with the theoretical contour length of PF2 (~103 nm), corresponding to a polymer with 29 repeating units (see Supporting Information). This strong correlation confirms that the observed domains originate from the donor phase and highlights the ability of sMIM to achieve chain-level resolution in identifying conductive polymer domains in bulk heterojunction blends.

From the morphological characterization, the choice of solvent affects the molecular packing and aggregation within the PF2:ITIC blend films. Consequently, the solvent is expected to further affect their optical properties. Fig. 5a displays the UV–visible absorption spectra of the films processed from the three different solvents.

All three films exhibit broad absorption in the 400–780 nm range, which closely matches the emission spectra of typical indoor light

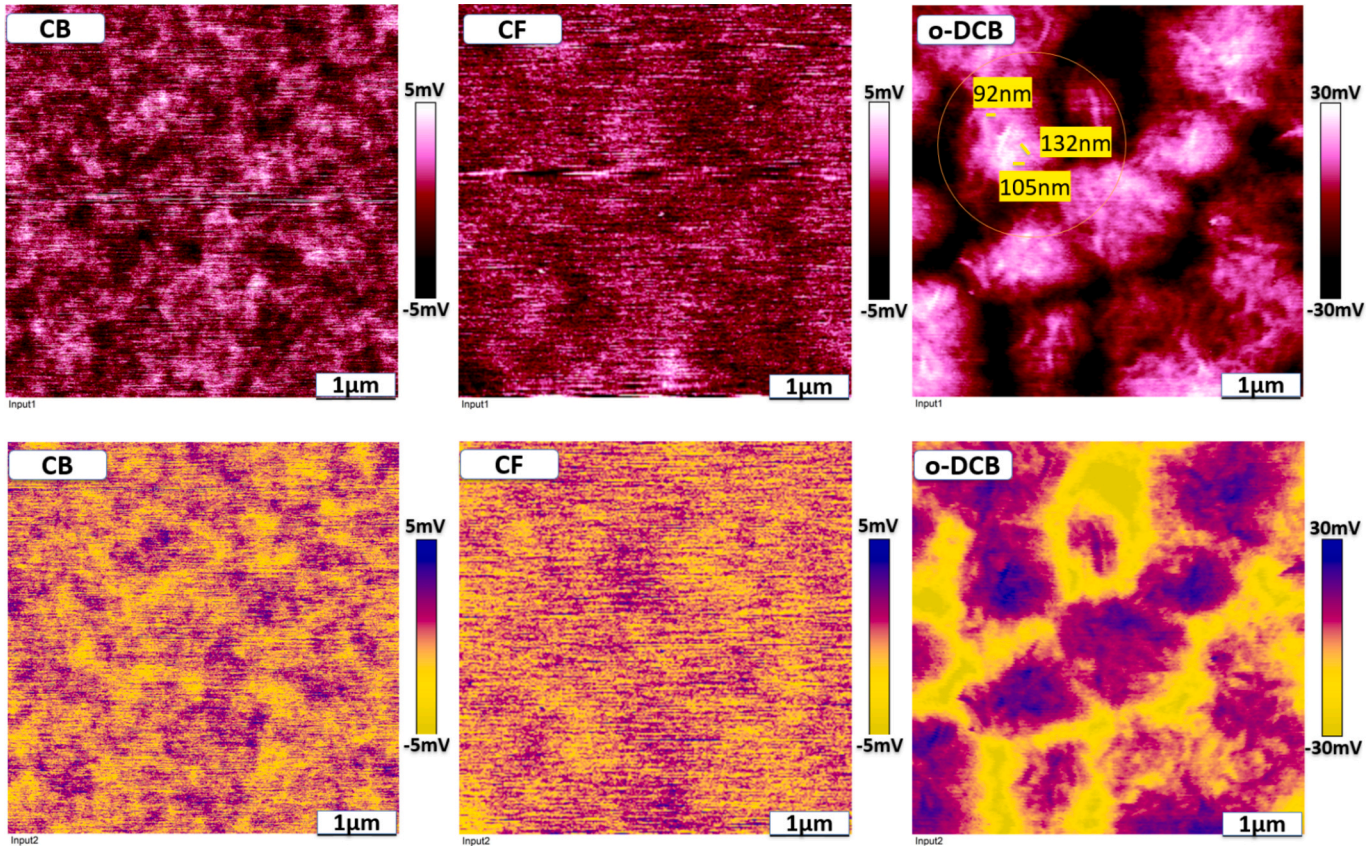

Fig. 4. sMIM-conductivity images (5 × 5 μm, top row), and sMIM-capacitance images (5 × 5 μm, bottom row) of PF2:ITIC films processed with CB, CF, and o-DCB.

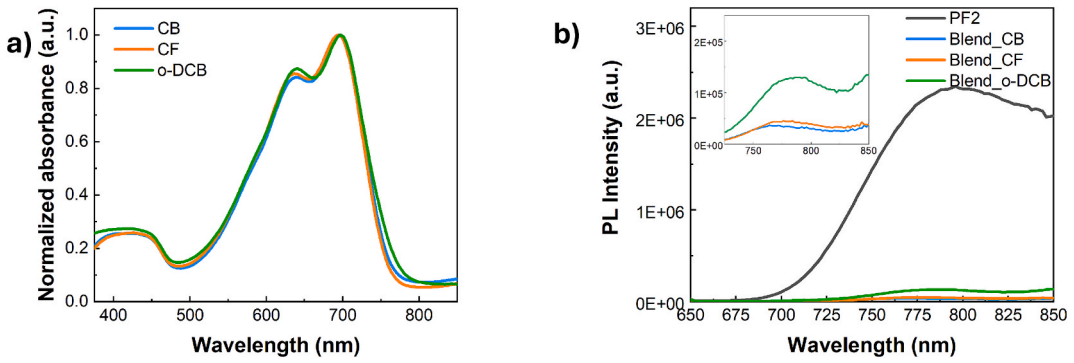

Fig. 5. (a) Normalized absorbance spectra of PF2:ITIC films processed with CB, CF, and o-DCB. All spectra were normalized to their respective maximum absorbance (peak value = 1). (b) PL spectra of neat PF2 and PF2:ITIC blend films processed with CB, CF, and o-DCB under 640 nm light excitation. The PL spectra were corrected for differences in absorbed excitation light by normalizing the measured PL intensity by the absorbed fraction at 640 nm, $f_{abs} = 1 - 10^{-A_{640}}$, where A_{640} is the absorbance at 640 nm.

sources. The UV–visible absorption spectrum showed three characteristic peaks at 440 nm, 640 nm, and 700 nm. The peak at 440 nm is attributed to π-π* transitions within the PF2 polymer, which are usually associated with electronic transitions in the conjugated polymer backbone and are particularly important for collecting blue region photons that are critical to indoor OPV performance. The peaks at 640 nm and 700 nm may be due to intramolecular charge transfer (ICT) transitions that occur between electron-rich and electron-deficient units [33,34]. In PF2, the presence of fluorinated side chains strengthens the ICT transitions, compared to non-fluorinated analogues [35]. In all solvents, the absorption peak position remains essentially unchanged, with only minor changes in intensity. Although UV–vis absorption confirmed that all blends had similar light harvesting capabilities, additional insights can be gained by examining their photoluminescence responses (Fig. 4b). The excitation wavelength was set to 640 nm, ensuring that both donor and acceptor were excited and allowing us to probe radiative recombination pathways. The film treated with CB exhibits the lowest PL intensity, indicating the most efficient exciton quenching, which in turn indicates the most efficient exciton dissociation and charge transfer to ITIC. In contrast, the films treated with CF and o-DCB exhibited higher PL intensities, indicating a lower efficiency of exciton quenching. These results are consistent with the morphological observations, where films treated with CF and o-DCB exhibited increased aggregation and surface roughness, likely reducing the donor–acceptor interfacial area. The reduction of interface density will limit the diffusion of excitons to the interface, resulting in increased recombination losses. Thus, the combined optical and morphological analyses highlight that CB enables superior donor–acceptor interactions, promotes efficient charge separation, and contributes to the overall enhanced photovoltaic performance observed in CB-treated devices.

Following the morphological and optical investigations on the PF2:ITIC blends, we subsequently fabricated OPV devices in the classical

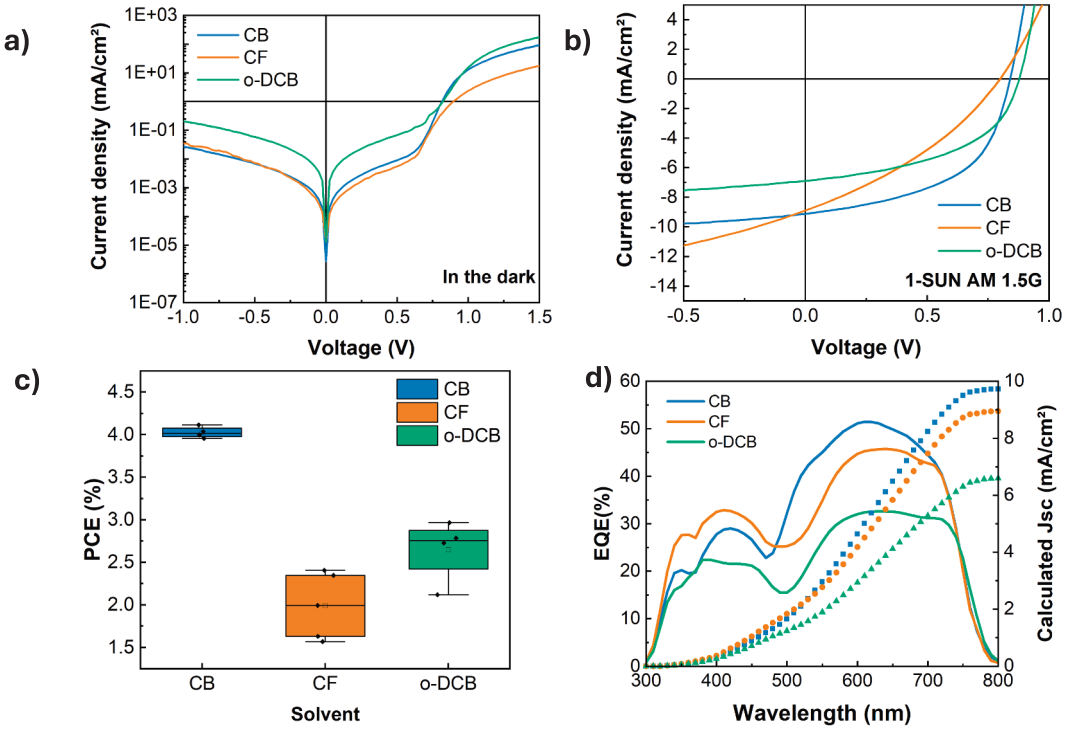

Fig. 6. (a) J-V curves of representative PF2:ITIC OPVs showing typical device performance in the dark in semi-logarithm scale. (b) Under solar simulator (100 mW. cm^{-2}); (c) Dispersion of PCE of six PF2:ITIC OPVs processed with CB, CF, and o-DCB under standard AM 1.5G illumination. (d) EQE spectra showing wavelength-integrated photocurrent through integration over the standard solar spectrum.

inverted architecture based on glass-ITO/ZnO/PF2:ITIC/MoO_3/Ag. Conventional current–density/voltage (J-V) characterizations and EQE analysis were used to evaluate the photovoltaic properties of PF2:ITIC-based solar cells, initially under standard AM1.5G (100mW. cm^{-2}) illumination, as shown in Fig. 6 and Table 1.

In the dark J-V curve (Fig. 6a), all devices exhibit a clear diode-like behavior, with the CB- and CF-treated devices showing low leakage currents under reverse bias. In contrast, the o-DCB device presents a significantly higher leakage current, which may result from structural discontinuities and poor phase separation, as previously observed in morphology studies. The steeper slope in the high forward bias region for the CB device confirms its lower R_S, while the slope at reverse bias confirms the higher R_{SH}, both of which indicate efficient charge transfer and minimal recombination rate. Under simulated standard AM1.5G illumination (Fig. 6b), the CB-treated device exhibits the highest J_{SC} and FF, confirming its superior photovoltaic behavior. Quantitatively, it delivers a J_{SC} of 9.0 mA/cm^2, FF of 55.4%, and a V_{OC} of 0.83 V, slightly higher than the 0.80 V typically obtained for PM6:Y6 reference systems. In addition, the lower R_S (30 Ω.cm^2) and higher R_{SH} (4700 Ω.cm^2) values in the CB-based devices further support the improvement in carrier extraction and suppression of charge recombination. In comparison, the CF- and o-DCB-processed devices exhibit lower photocurrents and poorer diode characteristics, consistent with their more disordered and aggregated morphologies. Device performance statistics are summarized in the box plot (Fig. 6c). The CB-based devices show the highest average PCE of 4.1% with minimal variation across six devices, indicating excellent reproducibility and morphological uniformity at the laboratory scale. By contrast, CF- and o-DCB-based devices yield lower PCEs of 2.4% and 3.0%, respectively, and larger standard deviations, reflecting less optimal and less consistent film formation. The EQE spectra and the calculated integrated J_{SC} values are presented in Fig. 6d. The EQE curve of the CB-treated device covers a broad spectral range with a high response between 400–750 nm, consistent with its superior photocurrent. The integrated J_{SC} values derived from EQE measurements are in good agreement with the J-V results, further validating the accuracy of the extracted device performance. The enhanced EQE and photovoltaic parameters of the CB-treated films are attributed to their favorable nanomorphology, which facilitates balanced charge transport, and minimizes charge recombination.

After studying the behavior of the PF2:ITIC-based devices under AM1.5G illumination, we further evaluated their performance under indoor low-power illumination. For this study, a warm white LED was used as the indoor light source, and its emission spectrum is presented in Supporting Information (Fig. S2). The power density was calibrated at 0.31 mW.cm^{-2} at 1000 lx, thanks to a dedicated calibrated and certified optical spectrometer. The J-V characteristics of the devices under indoor illumination (1000 lx) are shown in Fig. 7, and the corresponding extracted performance parameters are summarized in Table 2.

The maximum PCEs of PF2:ITIC OPVs processed with CB, CF, and o-DCB under 1000 lx warm LED illumination are 10.7%, 6.4%, and 6.0%, respectively, consistent with the averaged values reported in Table 2. Similar to the results obtained under AM1.5G, the CB-based device outperforms the others, with higher V_{OC} and J_{SC} compared to CF and o-DCB. The reduced J_{SC} of CF and o-DCB is attributed to the lower efficiency of exciton dissociation, charge recombination rate and charge carrier transport, which is consistent with the morphology and PL results discussed previously. To verify indoor performance, theoretical J_{SC} were calculated by combining the EQE spectrum of each device (Fig. 6b) with the irradiance spectrum of the 1000 lx warm LED. The calculated J_{SC} are 71.2 μA.cm^{-2} for CB, 65.7 μA.cm^{-2} for CF, and 46.8 μA.cm^{-2} for o-DCB, which are highly consistent with the experimental J_{SC} values reported in Table 2, confirming the reliability of the experimental results. Under indoor lighting, the photocurrent is significantly lower, the impact of R_S on device performance decreases, and R_{SH} becomes critical as it directly affects leakage current and recombination. Compared with CF and o-DCB devices, CB-treated devices showed lower R_S (800 Ω.cm^2) and significantly higher R_{SH} (~6×10^5 Ω.cm^2). This high R_{SH} value is critical to minimizing leakage in low light conditions and helps maintain high V_{OC} and FF. As reported in studies [14,36], R_{SH} varies more significantly with light intensity than R_S, and its magnitude strongly affects the behavior of V_{OC} and FF in indoor applications.

Before evaluating the effect of active layer thickness, we also examined the influence of the donor-to-acceptor (D:A) ratio in the active layer on device performance. Two different ratios, 1:1 and 1:1.5, were tested using CB as the solvent. While both ratios yielded similar V_{OC} and FF values, the 1:1.5 ratio resulted in slightly higher J_{SC} and PCE under indoor illumination. This enhancement may be attributed to improved donor–acceptor intermixing or enhanced percolation pathways for charge transport. Based on this observation, the 1:1.5 ratio was selected for the subsequent thickness optimization study. Detailed photovoltaic parameters are provided in Supporting Information (Table S3).

The active layer thickness in OSCs is a key parameter affecting the interplay between light absorption and charge transport, both of which are crucial for achieving high device efficiency, especially under low-intensity illumination. In organic semiconductors, the exciton diffusion length limits the effective size of donor–acceptor (D/A) domains. Smaller domains promote more efficient exciton dissociation at the D/A interface. However, the total active layer thickness is limited by the carrier diffusion length, which is controlled by the mobility and lifetime of the free charge carriers. In conventional OSCs, the active layer is usually limited to about 100 nm due to the moderate mobility of charge carriers, which restricts efficient charge extraction at larger thicknesses. Efficient transport in thicker layers requires a highly bi-continuous network to facilitate charge movement to the electrodes without significant recombination. Theoretical studies [37–39] have shown that if the carrier mobility is high enough, thicker active layers can simultaneously enhance photon absorption and efficient charge collection, thus potentially improving device performance without sacrificing efficiency. Moreover, from the technological point of view, processing thick active layers is crucial towards high throughput production based on printing technologies.

Before going to thick active layer using the PF2:ITIC blends, we first evaluated their hole mobilities from space-charge limited current (SCLC) measurements (see Supporting Information S7). The PF2:ITIC blend exhibits a relatively high hole mobility estimated at (1.49 ± 0.18) $\times 10^{-4}$ $cm^2.V^{-1}.s^{-1}$, indicating efficient charge transport through the active layer. This relatively high mobility supports the use of thick active layers (>100 nm), as charge carriers can move efficiently without significant trapping or recombination. Furthermore, PF2 has previously shown good mobility even when blended with $PC_{71}BM$ with thicknesses up to 265 ± 5 nm [20,40], further confirming its robustness in thicker film configurations. This property is particularly beneficial for IPV applications, as indoor light intensity is significantly lower than outdoor

Table 1
Photovoltaic parameters of PF2:ITIC inverted devices under outdoor standard illumination (AM1.5G, 100mW.cm^{-2}). The active layer is around 0.18 cm^2. Average J_{SC} and PCE are given in brackets. The average parameters were calculated from 6 cells, and the error estimate was calculated as the standard deviation of these 6 cells. J_{SC}^{EQE} is deduced from the EQE, by integrated over the reference solar spectrum (IEC 60904-3).

Solvent	V_{oc} (V)	J_{sc} (mA.cm^{-2})	J_{sc}^{EQE} (mA.cm^{-2})	FF (%)	PCE (PCE_{ave}) (%)	R_s (Ω.cm^2)	R_{sh} (Ω.cm^2)
CB	0.83	9.0 (9.1 ± 0.3)	9.7	55.4	4.1 (4.0 ± 0.1)	30	4700
CF	0.80	8.9 (7.8 ± 1.1)	9.3	33.8	2.4 (2.0 ± 0.4)	140	1200
o-DCB	0.88	6.9 (6.7 ± 0.2)	6.6	49.1	3.0 (2.7 ± 0.4)	20	4500

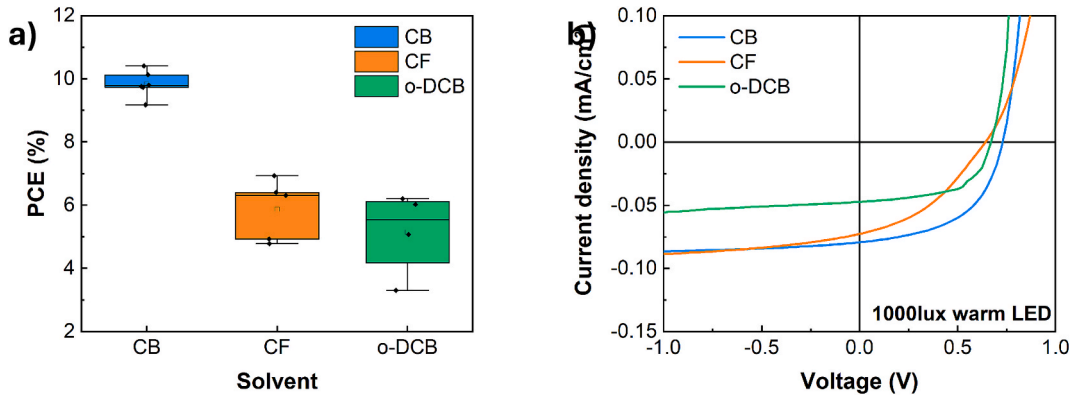

Fig. 7. (a) Dispersion of PCE of six PF2:ITIC OPVs processed with CB, CF, and o-DCB under 1000 lx warm LED illumination. (b) J-V curves of representative PF2:ITIC OPVs showing device performance under 1000 lx warm LED illumination.

Table 2
PV Parameters of the PF2:ITIC devices under 1000 lx warm LED Illumination.

Solvent	V_{oc} (V)	J_{sc} (μA. cm^{-2})	J_{sc}^{EQE} (μA. cm^{-2})	FF (%)	PCE (PCE_{ave}) (%)	R_s (Ω. cm^2)	R_{sh} (Ω. cm^2)
CB	0.73	76.3	71.2	56.6	10.7 (10.0 ± 0.5)	6×10^2	6×10^5
CF	0.64	72.7	65.7	38.5	6.4 (5.9 ± 1.0)	2×10^4	2×10^5
o-DCB	0.68	47.3	46.8	58.8	6.0 (5.2 ± 1.3)	4×10^2	3×10^5

conditions. In such low-light environments, thicker active layers can absorb more light, thereby improving the overall device performance [41,42]. To explore the practical potential of increasing the film thickness, we prepared PF2:ITIC hybrid films with a thickness close to 270 nm. The mixed solution was CB-based with a donor-to-acceptor ratio of 1:1.5 and a total concentration of 17.5 mg mL^{-1}. This is the same solution used for the thinner active layer devices discussed in the previous section; the difference in thickness was solely achieved by adjusting the spin-coating parameters.

AFM measurements (Fig. 8) show that both 100 nm and 270 nm PF2:ITIC films exhibit smooth and uniform surfaces with clear nanoscale morphology. The RMS roughness is comparable, 1.98 nm for the 100 nm film and 1.92 nm for the 270 nm film, indicating that increasing the thickness does not significantly change the surface topography. AFM adhesion images show consistent interpenetrating networks in both films, indicating that the donor–acceptor phase separation remains stable and well-structured at different thicknesses.

Photovoltaic parameters under standard AM 1.5G illumination (Table 3) demonstrate that both devices maintain the same open-circuit voltage (V_{OC} = 0.82 V), indicating similar energy alignment and negligible increase in recombination. However, increasing the active layer thickness results in a higher short-circuit current density (J_{SC} = 10.7 vs. 9.4 mA·cm^{-2}) and a slightly increased PCE (4.3% vs. 4.1%), despite a drop in fill factor (FF = 48% vs. 54%). The reduced FF can be attributed to increased series resistance and decreased shunt resistance in thicker devices, as confirmed by the dark J-V curves (Fig. 9c), which show higher leakage currents in the 270 nm devices. Under indoor LED illumination at 1000 lx (Fig. 9b), the advantage of the thicker active layer becomes even more apparent, where artificial light sources such as LEDs typically emit a large portion of their spectral power in the blue region. Specifically, blue photons (400–500 nm) represent approximately 14% of the total spectral power in warm LEDs, compared to as much as 38% in cold LEDs. The 270 nm device achieves a J_{SC} of 86.6 μA·cm^{-2} and a PCE of 12.0%, compared to 73.3 μA·cm^{-2} and 10.7% for the 100 nm device. Both devices maintain high FF and stable V_{OC} under low light, confirming efficient charge extraction even in weak lighting environments. EQE measurements (Fig. 9d) support these observations, showing a significant enhancement in external quantum efficiency in the blue spectral region (400–500 nm) for the thicker device. This enhancement aligns with the absorption spectra (Fig. 9a), which reveal that the increased thickness primarily improves light harvesting in the blue region, while absorption in the 500–700 nm range remains nearly unchanged. This indicates that photon collection in the 500–700 nm range is already saturated at 100 nm, while blue light absorption benefits significantly from the thicker active layer.

The photovoltaic performance of PF2:ITIC devices with different active layer thicknesses (100 nm and 270 nm) was further investigated under indoor warm LED lighting (ranging from 200 to 1000 lx). As shown in Fig. 10a, the J-V characteristics show that the current density gradually increases with the illumination, which is consistent for devices of both thicknesses.

Devices with a thickness of 270 nm consistently exhibit higher current density than those with 100 nm, which is consistent with the idea that a thicker active layer can absorb more photons and thus generate more charge carriers. Fig. 10b shows the log–log relationship between J_{SC} and the incident optical power density (P_{IN}). In both thickness (100 nm and 270 nm), the slope is close to 1, indicating a proportional relationship and suggesting efficient charge generation with minimal recombination losses. This linear dependence confirms that device operate in a recombination-free regime, even under low-light indoor conditions. This characteristic makes the PF2:ITIC blend particularly suitable for indoor photovoltaic applications. As shown in Table 4, the device with a 270 nm active layer achieves higher J_{SC} and PCE under all illumination conditions compared to the device with a 100 nm thickness. At 1000 lx, the PCE of the thicker device reaches 11.7%, while the thinner device reaches 10.0%. Even at the lowest tested illumination of 200 lx, the PCE of the 270 nm device remains above 11%, confirming the effectiveness of the thicker active layer in enhancing light absorption and charge collection at reduced photon flux. These findings highlight the potential of PF2:ITIC blends with increased active layer thickness to deliver high performance under various indoor lighting conditions, making them promising candidates for energy harvesting in low-light environments.

These results were obtained under warm white LED lighting, which was used throughout the illuminance-related tests to simulate indoor environments in IoT applications. Since PF2 absorbs blue light, and cold LEDs typically contain more short-wavelength photons, cold light can theoretically generate higher photocurrent. This study focused on a fixed and realistic indoor spectrum in order to isolate the effects of processing (solvent-dependent morphology) and active layer thickness on charge generation, transport, and recombination. Based on these findings, we anticipate that cold illumination may further enhance the photocurrent of PF2:ITIC devices. A systematic comparison between

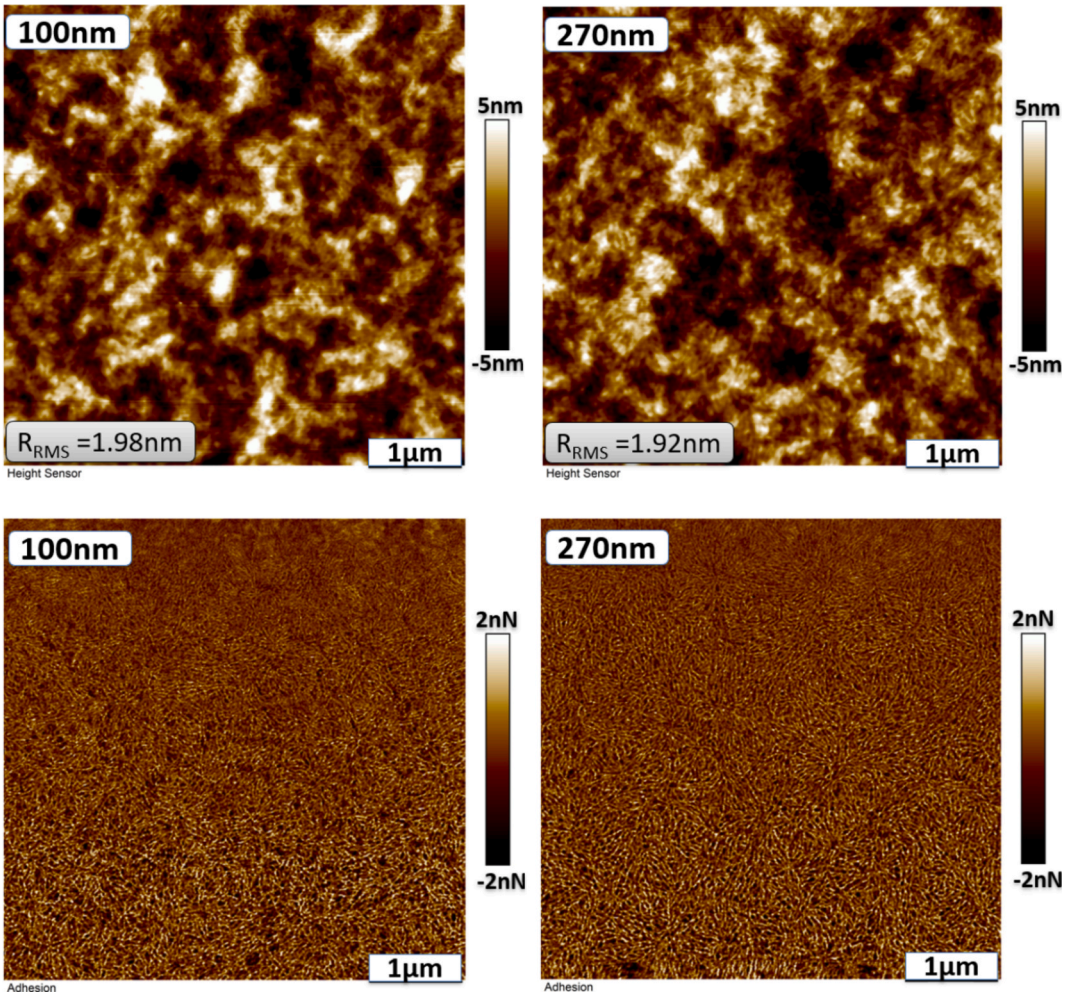

Fig. 8. AFM height images and AFM adhesion images of PF2:ITIC blend films with thicknesses of 100 nm and 270 nm.

Table 3
Photovoltaic parameters of PF2:ITIC devices with 100 nm and 270 nm active layer thicknesses under 1 sun (AM1.5G at 100 mW·cm^{-2}) and warm LED illumination (1000 lx). Values in parentheses represent the average ± standard deviation from six independently fabricated devices.

Thickness (nm)	Light source	V_{oc} (V)	J_{sc}	FF (%)	PCE (PCE_{ave}) (%)	R_s (Ω. cm^2)	R_{sh} (Ω. cm^2)
100	1 sun	0.82	9.4 mA cm^{-2}	54	4.1 (4.0 ± 0.1)	30 ± 1	3400 ± 200
	LED 1000 lx	0.70	73.3 µA cm^{-2}	61	10.7 (10.0 ± 0.5)	800 800 ± 30	6×10^5 (6 ± 3)× 10^5
270	1 sun	0.82	10.7 mA cm^{-2}	48	4.3 (4.1 ± 0.2)	50 50 ± 5	2900 2900 ± 300
	LED 1000 lx	0.72	86.6 µA cm^{-2}	59	12.0 (11.6 ± 0.2)	750 800 ± 100	6×10^5 (6 ± 1)× 10^5

warm and cold LEDs will be conducted in future studies.

4. Conclusion

In summary, to realize high-efficiency IOPVs with strong blue-light harvesting and high V_{OC}, we developed and optimized the PF2:ITIC-based active layer system thanks to the very specific absorption of the polymer fluorinated polymer donor in the blue region of the spectrum, matching the emission spectra of indoor LED lighting. By selecting chlorobenzene as the processing solvent, a uniform and defect-free morphology was achieved, enabling efficient exciton dissociation and charge transport. The morphology of the bulk heterojunction was found to be strongly dependent on solvent selection, not only through solubility but also via specific solvent-polymer interactions that influence crystallinity and phase separation. Increasing the active layer thickness to 270 nm enhanced light absorption in the blue region (400–500 nm), resulting in improved photocurrent generation. Under warm LED illumination at 1000 lx, the optimized PF2:ITIC devices delivered a high PCE of 12.0% and a V_{OC} of 0.72 V, which compares favorably in terms of voltage to the reference cell based on PM6:Y6 The combination of broad spectral absorption, high open-circuit voltage, and morphological robustness makes PF2 a promising donor candidate for high-performance indoor OPVs. This study demonstrates that with proper material selection and structural tuning, PF2-based systems can serve as effective platforms for indoor energy harvesting and potentially for integration in large-area printed photovoltaic applications.

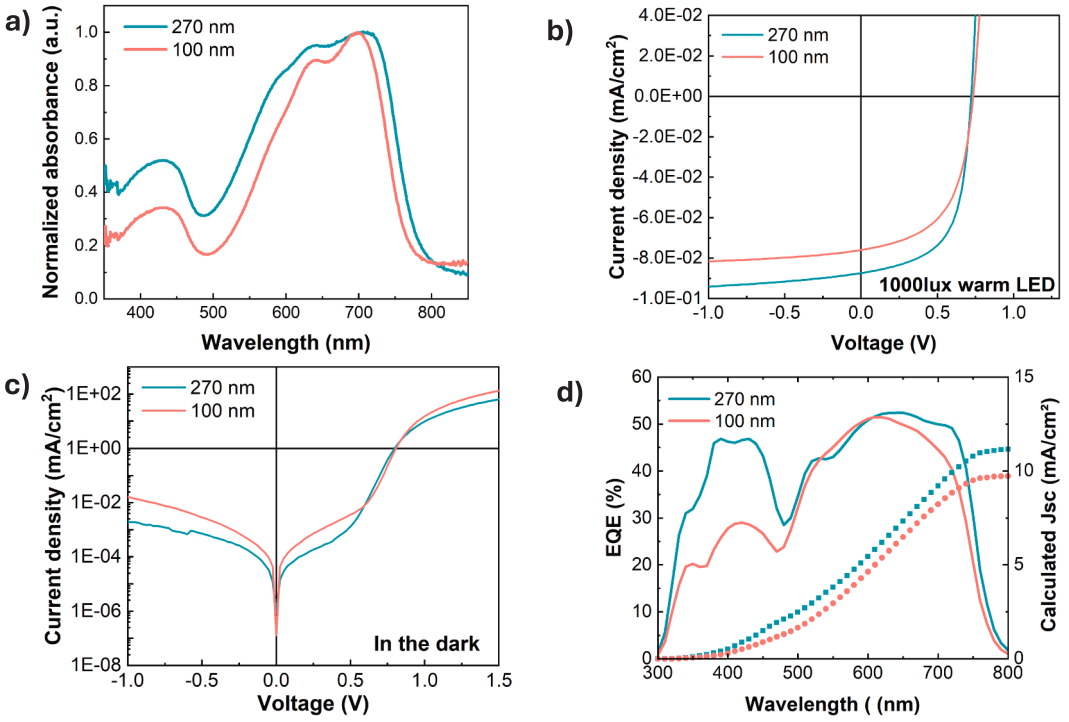

Fig. 9. Optical and electrical characterization of PF2:ITIC solar cells with active layer thicknesses of 100 nm and 270 nm. All spectra were normalized to their respective maximum absorbance (peak value = 1). (a) Absorption spectra of the active layers (each spectrum normalized to its maximum absorbance, peak value = 1). (b) J-V characteristics under warm LED (1000 lx). (c) J-V characteristics in the dark. (d) EQE spectra and integrated JSC values.

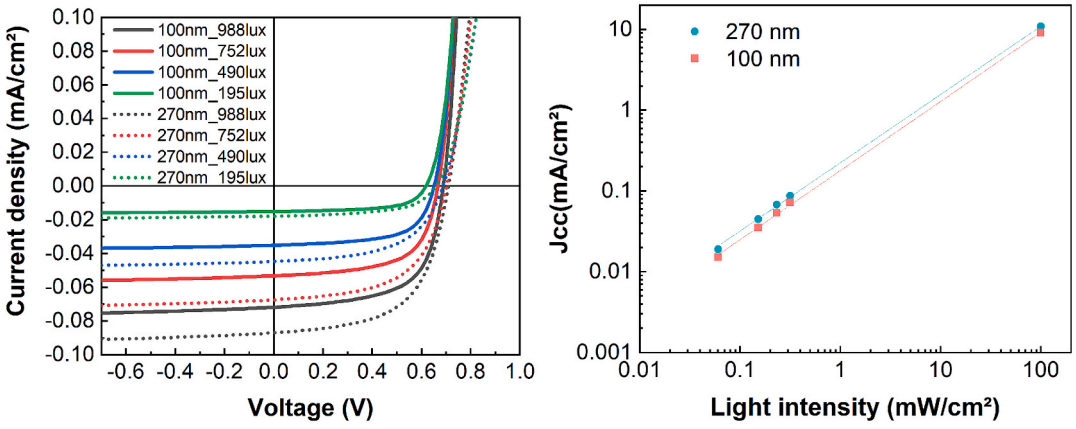

Fig. 10. (a) The corresponding J-V curves of PF2:ITIC with different thicknesses under indoor illumination from 200 to 1000 lx at warm LED. (b) Relationship between the J_{SC} and the P_{IN} for different thicknesses of the active layer (100 nm and 270 nm).

Table 4
Photovoltaic performance of PF2:ITIC with different active-layer thicknesses under warm LED illumination at illuminance levels from 200 to 1000 lx. R_S and R_{SH} (Ω.cm^2) are effective values extracted from the illuminated J-V characteristics and may vary slightly between measurement sessions.

Thickness (nm)	Conditions (lux)	V_{oc} (V)	J_{sc} (μA.cm^{-2})	FF (%)	PCE (PCE_{ave}) (%)	R_s (Ω.cm^2)	R_{sh} (Ω.cm^2)
100	1000	0.68	71.9	63.6	10.0	2.0×10^2	1.0×10^6
	750	0.66	53.2	63.0	9.5	2.6×10^2	1.3×10^6
	500	0.66	35.1	62.3	9.5	3.0×10^2	1.9×10^6
	200	0.62	15.1	62.5	9.7	5.0×10^2	4.1×10^6
270	1000	0.72	87.0	59.5	11.7	4.0×10^3	7.9×10^5
	750	0.70	67.4	57.8	11.7	4.5×10^3	9.4×10^5
	500	0.68	44.8	56.3	11.3	7.7×10^3	1.3×10^6
	200	0.66	17.9	57.4	11.2	9.3×10^3	3.2×10^6

CRediT authorship contribution statement

Ruoxue He: Conceptualization, Data curation, Formal analysis, Investigation, Visualization, Writing – original draft. **Nicolas Leclerc:** Methodology, Resources, Writing – review & editing. **Pierre Nickmilder:** Methodology, Formal analysis, Writing – review & editing. **Philippe Leclère:** Methodology, Supervision, Writing – review & editing. **Bernard Ratier:** Conceptualization, Funding acquisition, Project administration, Supervision, Writing – review & editing. **Johann Bouclé:** Conceptualization, Funding acquisition, Project administration, Supervision, Writing – review & editing.

Declaration of competing interest

The authors declare the following financial interests/personal relationships which may be considered as potential competing interests: Ruoxue HE reports financial support was provided by National Research Agency (ANR). Ruoxue HE reports financial support was provided by French Ministry of Higher Education and Research (MESR). If there are other authors, they declare that they have no known competing financial interests or personal relationships that could have appeared to influence the work reported in this paper.

Acknowledgements

This research benefited from the support of the PLATINOM platform, with funding from Nouvelle Aquitaine council and the European Union under the PILIM program. The PLATINOM test facility of XLIM is a member of the CNRS RF-Net network (ANR-22PEFT-001). The authors would like to thank Lionel Rechignat and Nicolas Parou for their technical assistance within the PLATINOM platform. This work also received financial support from the EUR TACTIC graduate school (French National Research Agency grant reference ANR-18-EURE-0017) and from institutional doctoral funding provided by the French Ministry of Higher Education and Research (MESR). The research at UMONS was partly supported by F.R.S.-FNRS Grands Equipements program (IPANEMA) and PDR program (PiezoFlexoTronics).

Appendix A. Supplementary data

Supplementary data to this article can be found online at https://doi.org/10.1016/j.solener.2026.114733.

Data availability

The data that support the findings of this study are available from the corresponding author upon reasonable request.

References

[1] D. Müller, E. Jiang, P. Rivas-Lazaro, et al., Indoor photovoltaics for the internet-of-things – a comparison of state-of-the-art devices from different photovoltaic technologies, ACS Appl Energy Mater 6 (2023) 10404–10414, https://doi.org/10.1021/acsaem.3c01274.
[2] A. Chakraborty, G. Lucarelli, J. Xu, et al., Photovoltaics for indoor energy harvesting, Nano Energy 128 (2024) 109932, https://doi.org/10.1016/j.nanoen.2024.109932.
[3] J. Bouclé, D. Ribeiro Dos Santos, A. Julien-Vergonjanne, Doing more with ambient light: harvesting indoor energy and data using emerging solar cells, Solar 3 (2023) 161–183, https://doi.org/10.3390/solar3010011.
[4] K.S. Srivishnu, M.N. Rajesh, S. Prasanthkumar, et al., Photovoltaics for indoor applications: progress, challenges and perspectives, Solar Energy 264 (2023) 112057, https://doi.org/10.1016/j.solener.2023.112057.
[5] V. Pecunia, L.G. Occhipinti, R.L.Z. Hoye, Emerging indoor photovoltaic technologies for sustainable internet of things, Adv Energy Mater 11 (2021) 2100698, https://doi.org/10.1002/aenm.202100698.
[6] B.H.S. Miranda, L.D.Q. Corrêa, G.A. Soares, et al., Efficient fully roll-to-roll coated encapsulated organic solar module for indoor applications, Solar Energy 220 (2021) 343–353, https://doi.org/10.1016/j.solener.2021.03.025.
[7] T.H. Kim, N.W. Park, M.A. Saeed, et al., Record indoor performance of organic photovoltaics with long-term stability enabled by self-assembled monolayer-based interface management, Nano Energy 112 (2023), https://doi.org/10.1016/j.nanoen.2023.108429.
[8] S. Mori, T. Gotanda, Y. Nakano, et al., Investigation of the organic solar cell characteristics for indoor LED light applications, Jpn J Appl Phys 54 (2015), https://doi.org/10.7567/JJAP.54.071602.
[9] Y. Wang, T. Yang, W. Cai, et al., Defect passivation refinement in perovskite photovoltaics: achieving efficiency over 45% under low-light and low-temperature dual extreme conditions, Adv Mater 36 (2024) 2312014, https://doi.org/10.1002/adma.202312014.
[10] S. Zeiske, O.J. Sandberg, N. Zarrabi, et al., Direct observation of trap-assisted recombination in organic photovoltaic devices, Nat Commun 12 (2021), https://doi.org/10.1038/s41467-021-23870-x.
[11] M. Freunek, M. Freunek, L.M. Reindl, Maximum efficiencies of indoor photovoltaic devices, IEEE J Photovoltaics 3 (2013) 59–64, https://doi.org/10.1109/JPHOTOV.2012.2225023.
[12] I. Mathews, S.N. Kantareddy, T. Buonassisi, et al., Technology and market perspective for indoor photovoltaic cells, Joule 3 (2019) 1415–1426, https://doi.org/10.1016/j.joule.2019.03.026.
[13] Z. Ding, R. Zhao, Y. Yu, et al., All-polymer indoor photovoltaics with high open-circuit voltage, J Mater Chem A 7 (2019) 26533–26539, https://doi.org/10.1039/C9TA10040G.
[14] Y. Cui, Y. Wang, J. Bergqvist, et al., Wide-gap non-fullerene acceptor enabling high-performance organic photovoltaic cells for indoor applications, Nat Energy 4 (2019) 768–775, https://doi.org/10.1038/s41560-019-0448-5.
[15] S. Jung, J. Oh, U.J. Yang, et al., 3D Cu ball-based hybrid triboelectric nanogenerator with non-fullerene organic photovoltaic cells for self-powering indoor electronics, Nano Energy 77 (2020), https://doi.org/10.1016/j.nanoen.2020.105271.
[16] J. Liu, Y. Cui, Y. Zu, et al., Organic photovoltaic cells for low light applications offering new scope and orientation, Organic Electron 85 (2020), https://doi.org/10.1016/j.orgel.2020.105798.
[17] T. Liu, Q.C. Burlingame, M.R. Ivancevic, et al., Photochemical decomposition of Y-series non-fullerene acceptors is responsible for degradation of high-efficiency organic solar cells, Adv Energy Mater 13 (2023) 2300046, https://doi.org/10.1002/aenm.202300046.
[18] P. Weitz, V.M. Le Corre, X. Du, et al., Revealing photodegradation pathways of organic solar cells by spectrally resolved accelerated lifetime analysis, Adv Energy Mater 13 (2023) 2202564, https://doi.org/10.1002/aenm.202202564.
[19] S. Hwang, T. Yasuda, Indoor photovoltaic energy harvesting based on semiconducting π-conjugated polymers and oligomeric materials toward future IoT applications, Polym J 55 (2023) 297–316, https://doi.org/10.1038/s41428-022-00727-8.
[20] O.A. Ibraikulov, C. Ngov, P. Chávez, et al., Face-on orientation of fluorinated polymers conveyed by long alkyl chains: a prerequisite for high photovoltaic performances, J Mater Chem A 6 (2018) 12038–12045, https://doi.org/10.1039/c8ta04127j.
[21] O.A. Ibraikulov, J. Wang, N. Kamatham, et al., ITO-free organic photovoltaic modules based on fluorinated polymers deposited from non-halogenated solution: a major step toward large-scale module production, Solar RRL 3 (2019), https://doi.org/10.1002/solr.201900273.
[22] X. Ma, Q. An, O.A. Ibraikulov, et al., Efficient ternary organic photovoltaics with two polymer donors by minimizing energy loss, J Mater Chem A 8 (2020) 1265–1272, https://doi.org/10.1039/c9ta12025d.
[23] W. Zhao, D. Qian, S. Zhang, et al., Fullerene-free polymer solar cells with over 11% efficiency and excellent thermal stability, Adv Mater 28 (2016) 4734–4739, https://doi.org/10.1002/adma.201600281.
[24] Q. Fan, Z. Xu, X. Guo, et al., High-performance nonfullerene polymer solar cells with open-circuit voltage over 1 V and energy loss as low as 0.54 eV, Nano Energy 40 (2017) 20–26, https://doi.org/10.1016/j.nanoen.2017.07.047.
[25] Y. Wang, Q. Fan, X. Guo, et al., High-performance nonfullerene polymer solar cells based on a fluorinated wide bandgap copolymer with a high open-circuit voltage of 1.04 V, J Mater Chem A 5 (2017) 22180–22185, https://doi.org/10.1039/c7ta07785h.
[26] S. Grott, A. Kotobi, L.K. Reb, et al., Solvent tuning of the active layer morphology of non-fullerene based organic solar cells, Solar RRL 6 (2022), https://doi.org/10.1002/solr.202101084.
[27] Y. Lin, J. Wang, Z. Zhang, et al., An electron acceptor challenging fullerenes for efficient polymer solar cells, Adv Mater 27 (2015) 1170–1174, https://doi.org/10.1002/adma.201404317.
[28] Bede Pittenger, Erina N, Chanmin Su. Quantitative mechanical property mapping at the nanoscale with PeakForce QNM 2010. https://doi.org/10.13140/RG.2.1.4463.8246.
[29] U. Celano (Ed.), Electrical Atomic Force Microscopy for Nanoelectronics, Springer International Publishing, Cham, 2019, https://doi.org/10.1007/978-3-030-15612-1.
[30] Rubin KA. Scanning Microwave Impedance Microscopy (sMIM) in Electronic and Quantum Materials. In: Celano, U. (eds) Electrical Atomic Force Microscopy for Nanoelectronics. 2019.
[31] IEC-TS-62607-7-2-2023.pdf n.d.
[32] J. Wang, I. Rodriguez-Donis, S. Thiebaud-Roux, et al., Selection of green solvents for organic photovoltaics by reverse engineering, Mol Syst Des Eng 7 (2022) 182–195, https://doi.org/10.1039/D1ME00151E.
[33] Y. Zhong, L. Biniek, N. Leclerc, et al., Segregated versus disordered stacking in two low bandgap alternated copolymers for photovoltaic applications: impact of polymorphism on optical properties, Macromolecules 51 (2018) 4238–4249, https://doi.org/10.1021/acs.macromol.8b00378.

[34] T. Olla, O.A. Ibraikulov, S. Ferry, et al., Benzothiadiazole halogenation impact in conjugated polymers, a comprehensive study, Macromolecules 52 (2019) 8006–8016, https://doi.org/10.1021/acs.macromol.9b01760.
[35] J. Shin, M. Kim, J. Lee, et al., Positional effects of fluorination in conjugated side chains on photovoltaic properties of donor–acceptor copolymers, Chem Commun 53 (2017) 1176–1179, https://doi.org/10.1039/C6CC06646A.
[36] M.A. Saeed, S.H. Kim, H. Kim, et al., Indoor organic photovoltaics: optimal cell design principles with synergistic parasitic resistance and optical modulation effect, Adv Energy Mater 11 (2021) 2003103, https://doi.org/10.1002/aenm.202003103.
[37] J. Yuan, Y. Zhang, L. Zhou, et al., Single-junction organic solar cell with over 15% efficiency using fused-ring acceptor with electron-deficient core, Joule 3 (2019) 1140–1151, https://doi.org/10.1016/j.joule.2019.01.004.
[38] Q. Liu, Y. Jiang, K. Jin, et al., 18% Efficiency organic solar cells, Sci Bull 65 (2020) 272–275, https://doi.org/10.1016/j.scib.2020.01.001.
[39] D. Lübke, P. Hartnagel, M. Hülsbeck, et al., Understanding the thickness and light-intensity dependent performance of green-solvent processed organic solar cells, ACS Mater Au (2022), https://doi.org/10.1021/acsmaterialsau.2c00070.
[40] D. Zhang, B. Fan, L. Ying, et al., Recent progress in thick-film organic photovoltaic devices: materials, devices, and processing, SusMat 1 (2021) 4–23, https://doi.org/10.1002/sus2.10.
[41] H. Yin, L.-K. Ma, J. Yan, et al., Thick-film low driving-force indoor light harvesters, Solar RRL 4 (2020), https://doi.org/10.1002/solr.202000291.
[42] T. Wang, Z.-C. Wen, L.-H. Xu, et al., One-micron-thick organic indoor light harvesters with low photocurrent loss and fill factors over 67%, J Mater Chem A 9 (2021) 13515–13521, https://doi.org/10.1039/d1ta02345d.